



OPEN





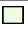











































MRI- and histologically derived neuroanatomical atlas of the *Ambystoma mexicanum* (axolotl)

Ivan Lazcano^{1✉}, Abraham Cisneros-Mejorado^{1,2}, Luis Concha¹, Juan José Ortiz-Retana¹, Eduardo A. Garza-Villarreal^{1✉} & Aurea Orozco¹

Amphibians are an important vertebrate model system to understand anatomy, genetics and physiology. Importantly, the brain and spinal cord of adult urodels (salamanders) have an incredible regeneration capacity, contrary to anurans (frogs) and the rest of adult vertebrates. Among these amphibians, the axolotl (*Ambystoma mexicanum*) has gained most attention because of the surge in the understanding of central nervous system (CNS) regeneration and the recent sequencing of its whole genome. However, a complete comprehension of the brain anatomy is not available. In the present study we created a magnetic resonance imaging (MRI) atlas of the in vivo neuroanatomy of the juvenile axolotl brain. This is the first MRI atlas for this species and includes three levels: (1) 82 regions of interest (ROIs) and a version with 64 ROIs; (2) a division of the brain according to the embryological origin of the neural tube, and (3) left and right hemispheres. Additionally, we localized the myelin rich regions of the juvenile brain. The atlas, the template that the atlas was derived from, and a masking file, can be found on Zenodo at <https://doi.org/10.5281/zenodo.4595016>. This MRI brain atlas aims to be an important tool for future research of the axolotl brain and that of other amphibians.

The Mexican axolotl *Ambystoma mexicanum*, (from the Nahuatl, "water monster") is a mythic native neotenic salamander that has amazed scientists initially for its peculiar life cycle¹ and later on for its tissue regeneration capacity², a trait lost later during vertebrate evolution. Specially interesting is the capacity of the axolotl to regenerate nervous tissue, which has been described for the pallium^{3,4}, the homologue of the cerebral cortex in mammals⁵, as well as for the spinal cord, both of which are able to regenerate after injury⁶. Although this capacity has placed axolotl as an animal model for neural regeneration studies, a thorough comprehension of the nervous system of this taxon remains obscure. In this context some axolotl brain structures have been well described by several authors⁵⁻⁷. In general terms, the juvenile-adult brain of axolotl (and other amphibians) is composed by regions similar to those of other vertebrates: olfactory bulb, telencephalon, diencephalon, mesencephalon, and rhombencephalon. Histological procedures provide excellent differentiation of tissue types, albeit having limited sampling of the three-dimensional spatial domain, and the introduction of deformations due to tissue handling. Magnetic resonance imaging (MRI) is a tool that allows the non-invasive assessment of the neuroanatomy of virtually any species that fits the scanner bore. MRI has been employed to generate in vivo and ex vivo atlases of the central nervous system (CNS) from different species, i.e., human⁸, rodent⁹⁻¹¹, avian^{12,13}, reptil^{14,15} as well as fish^{16,17}. With this in mind, and to further understand the species anatomy and function, we developed a MRI-based in vivo atlas of the juvenile *Ambystoma mexicanum* with the advantage of preserving the shape of its parenchyma, as well as vascular and ventricular systems and correlated this atlas with a histological visualization of myelin. The relevance of this atlas is that at this moment, an amphibian MRI atlas is not available; therefore, it will be an invaluable tool for comparative neuroanatomy, biologists, environmentalists or other researchers interested in this species and other amphibians. Moreover, the importance of axolotl as a model species stresses the importance of understanding different aspects of the biology of this species brought to danger of extinction (<https://www.iucnredlist.org/species/1095/53947343>).

¹Instituto de Neurobiología, Universidad Nacional Autónoma de México (UNAM), Campus Juriquilla, Santiago de Querétaro, Querétaro, México. ²CONACYT-Instituto de Neurobiología, Universidad Nacional Autónoma de México (UNAM), Campus Juriquilla, Santiago de Querétaro, Querétaro, México. ✉email: ivanlazcano@comunidad.unam.mx; egarza@comunidad.unam.mx

Structure	Abbreviation	Hemisphere	Mayor structure	Mean volume (mm ³)	SD	Color
Olfactory nerve	on ¹⁹	Left	Olfactory bulb	0.161	0.028	
Glomerular layer	g ¹⁹	Left	Olfactory bulb	0.472	0.077	
Mitral cell layer	m ¹⁹	Left	Olfactory bulb	0.24	0.031	
Granule cell layer	gc ¹⁹	Left	Olfactory bulb	0.116	0.018	
Anterior olfactory nucleus	aon ¹⁹	Left	Olfactory bulb	0.139	0.016	
Pallium	p ²⁰	Left	Telencephalon	0.337	0.046	
Accessory olfactory bulb	aob ²⁰	Left	Telencephalon	0.442	0.06	
Dorsal pallium	dp ^{4,20}	Left	Telencephalon	0.83	0.14	
Lateral pallium	lp ^{4,20}	Left	Telencephalon	0.942	0.144	
Medial pallium	mp ^{4,20}	Left	Telencephalon	0.732	0.129	
Septum	s ^{4,20,21}	Left	Telencephalon	0.668	0.094	
Striatum	str ^{4,20,21}	Left	Telencephalon	0.511	0.06	
Medial part of amygdala	amc ^{22,23}	Left	Telencephalon	0.068	0.009	
Pallial commissure	cpa ²³	Left	Telencephalon	0.02	0.004	
Anterior commissure	ca ²³	Left	Telencephalon	0.025	0.003	
Anterior preoptic nucleus	npa ^{23,24}	Left	Telencephalon	0.101	0.01	
Lateral/medial forebrain bundle	lfb ²⁴	Left	Telencephalon	0.702	0.083	
Choroid plexus	cp ³	Left	Telencephalon	0.171	0.034	
Thalamic eminence	em th ²³	Left	Telencephalon	0.025	0.005	
Posterior preoptic nucleus	ppn ²³	Left	Diencephalon	0.068	0.009	
Habenula	hab ^{21,24}	Left	Diencephalon	0.041	0.005	
Dorsal thalamus	dth ^{21,24}	Left	Diencephalon	0.508	0.052	
Ventral thalamus	vth ^{21,24}	Left	Diencephalon	0.193	0.028	
Hypothalamus dorsalis	hyth d ^{21,24}	Left	Diencephalon	0.872	0.105	
Paraventricular organ	pvo ^{21,24}	Left	Diencephalon	0.052	0.008	
Pars dorsalis hypothalami	pdh ^{21,24}	Left	Diencephalon	0.025	0.004	
Pars ventralis hypothalami	pvh ^{21,24}	Left	Diencephalon	0.025	0.002	
Subcommissural organ	so ^{21,24}	Left	Diencephalon	0.019	0.003	
Ependymal cell layer	ecl ²⁴	Left	Diencephalon	0.254	0.232	
Optic chiasm	och ²⁴	Left	Mesencephalon	0.023	0.003	
Optic tectum	to ^{21,24}	Left	Mesencephalon	0.774	0.118	
Tegmentum	tgm ^{21,24}	Left	Mesencephalon	0.482	0.058	
Nucleus interpeduncularis	nip ²¹	Left	Mesencephalon	0.005	0.002	
Hypothalamus ventralis	hyt v ²¹	Left	Mesencephalon	0.193	0.028	
Pituitary	hy ^{25,26}	Left	Endocrine	0.086	0.02	
Medulla oblongata	mo ²⁵	Left	Rombencephalon	0.36	0.044	
Cerebellum	cb ^{25,26}	Left	Rombencephalon	0.157	0.018	
Nervous trigeminus	V ²¹	Left	Rombencephalon	0.078	0.016	
Nervous lateralis anterior/nervous octavus	VIII ²¹	Left	Rombencephalon	0.171	0.028	
Gray matter of medulla oblongata	gmob ²⁵	Left	Rombencephalon	0.685	0.08	
White matter of medulla oblongata	wmob ²⁵	Left	Rombencephalon	1.403	0.155	
Olfactory nerve	on ¹⁹	Right	Olfactory bulb	0.193	0.032	
Glomerular layer	g ¹⁹	Right	Olfactory bulb	0.419	0.068	
Mitral cell layer	m ¹⁹	Right	Olfactory bulb	0.24	0.039	
Granule cell layer	gc ¹⁹	Right	Olfactory bulb	0.119	0.017	
Anterior olfactory nucleus	aon ¹⁹	Right	Olfactory bulb	0.142	0.016	
Pallium	p ²⁰	Right	Telencephalon	0.35	0.044	
Accessory olfactory bulb	aob ²⁰	Right	Telencephalon	0.413	0.059	
Continued						

Structure	Abbreviation	Hemisphere	Mayor structure	Mean volume (mm ³)	SD	Color
Dorsal pallium	dp ^{4,20}	Right	Telencephalon	0.844	0.15	■
Lateral pallium	lp ^{4,20}	Right	Telencephalon	0.878	0.144	■
Medial pallium	mp ^{4,20}	Right	Telencephalon	0.718	0.13	■
Septum	s ^{4,20,21}	Right	Telencephalon	0.675	0.084	■
Striatum	str ^{4,20,21}	Right	Telencephalon	0.464	0.054	■
Medial part of amygdala	amc ^{22,23}	Right	Telencephalon	0.07	0.013	■
Pallial commissure	cpa ²³	Right	Telencephalon	0.023	0.003	■
Anterior commissure	ca ²³	Right	Telencephalon	0.027	0.005	■
Anterior preoptic nucleus	npa ^{23,24}	Right	Telencephalon	0.108	0.015	■
Lateral/medial forebrain bundle	lfb ²⁴	Right	Telencephalon	0.72	0.093	■
Choroid plexus	cp ³	Right	Telencephalon	0.142	0.033	■
Thalamic eminence	em th ²³	Right	Telencephalon	0.024	0.004	■
Posterior preoptic nucleus	ppn ²⁴	Right	Diencephalon	0.07	0.008	■
Habenula	hab ^{21,24}	Right	Diencephalon	0.04	0.005	■
Dorsal thalamus	dth ^{21,24}	Right	Diencephalon	0.513	0.053	■
Ventral thalamus	vth ^{21,24}	Right	Diencephalon	0.174	0.029	■
Hypothalamus dorsalis	hyth d ^{21,24}	Right	Diencephalon	0.861	0.094	■
Paraventricular organ	pvo ^{21,24}	Right	Diencephalon	0.052	0.008	■
Pars dorsalis hypothalami	pdh ^{21,24}	Right	Diencephalon	0.022	0.004	■
Pars ventralis hypothalami	pvh ^{21,24}	Right	Diencephalon	0.026	0.002	■
Subcommissural organ	so ^{21,24}	Right	Diencephalon	0.019	0.003	■
Ependymal cell layer	ecl ²⁴	Right	Diencephalon	0.26	0.031	■
Optic chiasm	och ²⁴	Right	Mesencephalon	0.021	0.004	■
Optic tectum	to ^{21,24}	Right	Mesencephalon	0.765	0.132	■
Tegmentum	tgm ^{21,24}	Right	Mesencephalon	0.467	0.063	■
Nucleus interpeduncularis	nip ²¹	Right	Mesencephalon	0.004	0.002	■
Hypothalamus ventralis	hyt v ²¹	Right	Mesencephalon	0.551	0.067	■
Pituitary	hy ^{25,26}	Right	Pituitary	0.09	0.018	■
Medulla oblongata	mo ²⁵	Right	Rombencephalon	0.363	0.04	■
Cerebellum	cb ^{25,26}	Right	Rombencephalon	0.153	0.023	■
Nervous trigeminus	V ²¹	Right	Rombencephalon	0.07	0.009	■
Nervous lateralis anterior/nervous octavus	VIII ²¹	Right	Rombencephalon	0.154	0.022	■
Gray matter of medulla oblongata	gmob ²⁵	Right	Rombencephalon	0.687	0.076	■
White matter of medulla oblongata	wmob ²⁵	Right	Rombencephalon	1.349	0.151	■

Table 1. List of ROIs, abbreviations, references, hemisphere, mayor structure, volume, standard deviation (SD) and color.

Results and discussion

Although the brain of different vertebrates seems structurally different in morphology, it can be subdivided in the same way according to the embryonic origin of the neural tube. In particular, the amphibian brain has been studied in anatomical detail earlier and has been subdivided in olfactory bulb, telencephalon, diencephalon, mesencephalon, and rhombencephalon¹⁸. In the present work, we created an average template from 14 juvenile axolotls with a final voxel resolution of $0.040 \times 0.040 \times 0.040$ mm. We manually delineated 82 regions of interest (41 per hemisphere) for the 82-ROI atlas and 64 (32 per hemisphere) regions for the 64-ROI atlas. The average volume of each region as well as its variability are summarized in Table 1 and Supplementary Table 1. Whole brain volume per hemisphere (left: 13.4 1.66; right: 13.2 1.65) is shown in Supplementary Fig. 1. We manually segmented these regions based on previous annotations from axolotl histological studies in which techniques such as cresyl violet staining, immunohistochemistry or neuronal tracing were used Table 1. At the end of segmentation, we are able to create for the first time a MRI atlas of the axolotl brain (Fig. 1) in which subdivisions of the main structures present in other vertebrates can be observed (olfactory bulb, telencephalon, etc.). Moreover, we also segmented the pituitary gland, an endocrine organ which interacts directly and indirectly with the brain.

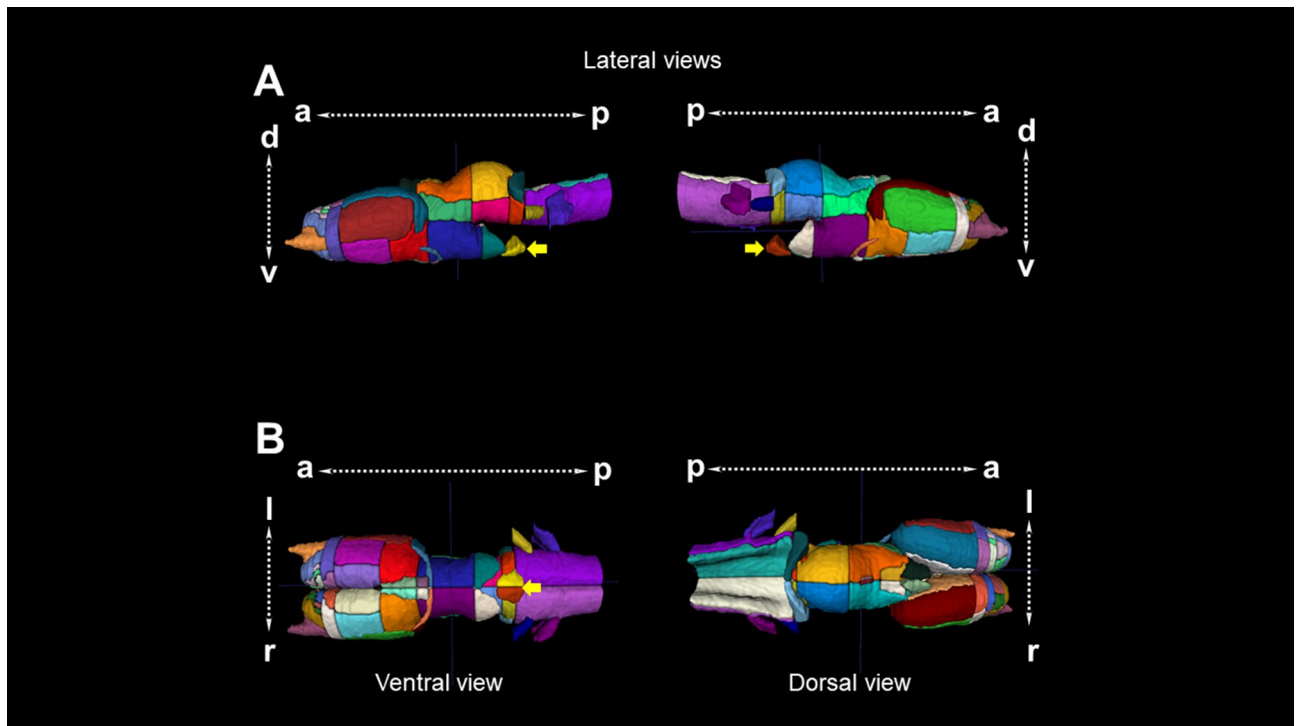


Figure 1. 3D reconstruction of the brain of *Ambystoma mexicanum* employing MRI. (A) Lateral views from the left and right sides of the complete 3D reconstruction created from our template. (B) Ventral (left) and dorsal (right) views of the complete 3D reconstruction. Every reconstruction shows each region in a different color when manual delineation was possible. Yellow arrows denote the pituitary gland.

Olfactory bulb. Employing previous information of the olfactory bulb structures, we are able to distinguish the olfactory nerve, the glomerular-, mitral- and granular cell layers and the anterior olfactory nucleus (Table 1, Fig. 2). These structures contribute to the integration of information coming from olfactory neuroreceptors from the nasal cavity. In mammals, some of the cell structures that contribute to integrate odorant signals are well documented in terms of morphology, connectivity and function²⁷, but information in amphibians is still scarce.

Telencephalon. This is the biggest brain structure in salamanders; the anterior part of the telencephalon contains the pallium and subpallium and the lateral ventricles. The pallium and subpallium comprise the left and right hemispheres. Axolotl pallium is interesting due to its capacity to regenerate after damage⁴, a trait probably present in other salamanders⁷. Because our MRI did not allow enough contrast to differentiate structures such as the dorsal pallium, lateral pallium, medial pallium and striatum and septum, we decided to further segment these regions manually using visual inspection from drawings in previous publications (Table 1). The lateral ventricles (not segmented) were hyperintense in terms of contrast in our T2-weighted MRI images and are depicted in Fig. 3A. The dorsal, lateral and medial pallium extend to the posterior part of the telencephalon but present a different morphology as compared with the anterior telencephalon structures. Moreover, at this brain location, the distance between the lateral ventricles (left and right) is reduced and even located adjacently at a more posterior region, finally forming the third ventricle (Fig. 3B). We segmented the amygdaloid complex, the lateral/medial forebrain bundle, the anterior preoptic nucleus, the thalamic eminence, and the pallial and anterior commissures, according to previous annotations (Fig. 3C). Moreover, the choroid plexus, which secretes cerebrospinal fluid into the vertebrate brain²⁸ was evident using MRI, contrary to what is observed in histological analysis due to the difficulty to preserve this structure.

Diencephalon. At the diencephalon level, we could identify two general structures, thalamus and dorsal hypothalamus (Fig. 4). We segmented the thalamus into dorsal and ventral thalamus. At the top of the dorsal thalamus, we identified the habenula (Fig. 4A) and the subcommissural organ (Fig. 4B). The habenula is a structure present in all vertebrates which participates in the integration of the limbic system, the basal ganglia and the sensory information²⁹. The subcommissural organ contains secretory ependymal cells located at the roof of the third ventricle³⁰. The contrast of the latter was hyperintense and centrally located with respect to the thalamus/hypothalamus. The dorsal hypothalamus includes nuclei that surround the floor of the third ventricle such as the posterior preoptic nucleus, paraventricular organ, pars dorsalis and pars ventralis hypothalami. All these regions have been recognized as neurosecretory cells which participate in neuroendocrine systems (Fig. 4A,B)³¹. Finally, the optic chiasm was also evident in our MRI images at the floor of the dorsal hypothalamus (Fig. 4A). In this region, it is well accepted that nerve fibers cross and allow binocular communication between eyes and the brain³²; however, this does not always occur in the vertebrate optic chiasm³³. In *Xenopus laevis*, for example, fiber

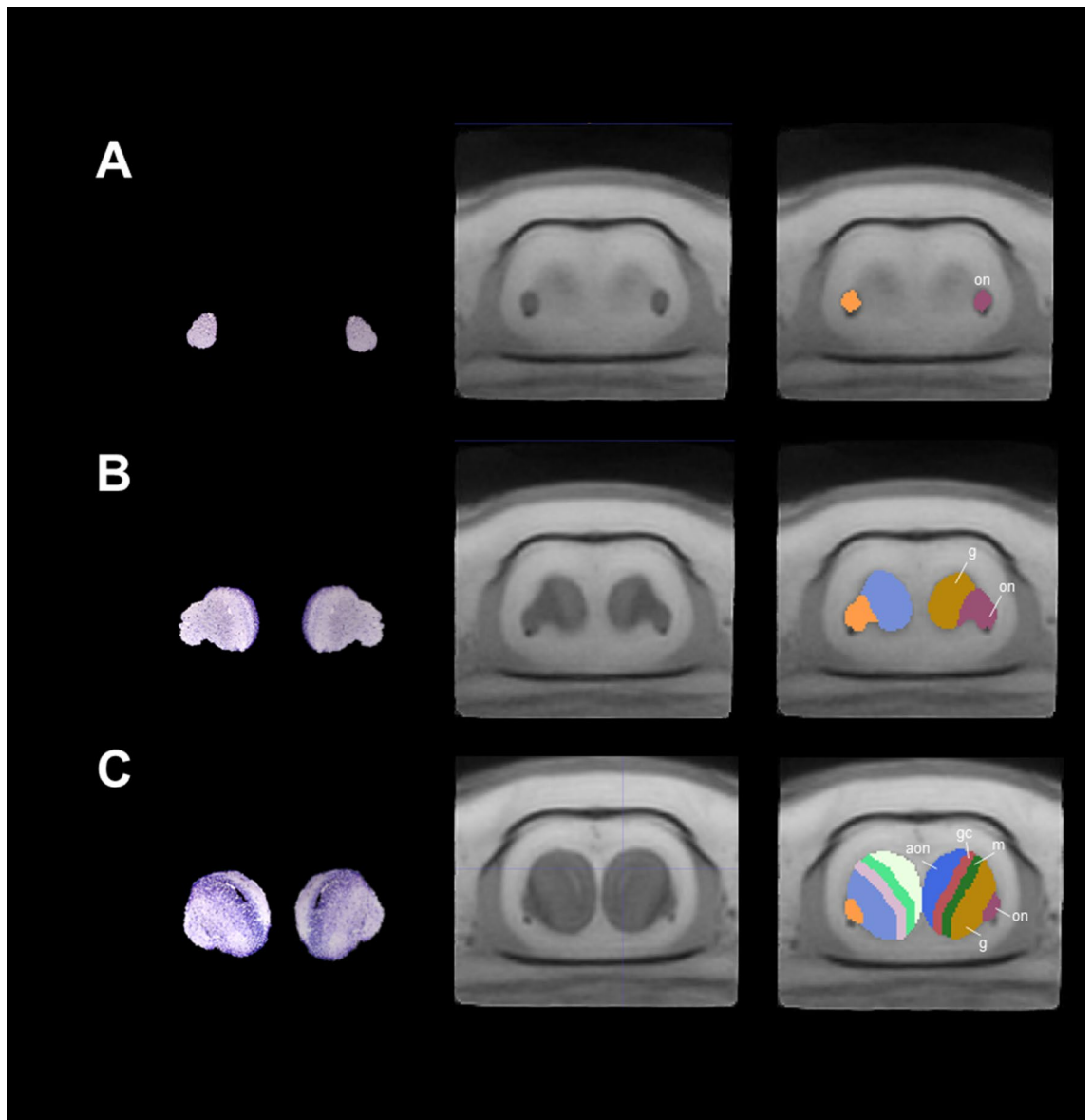


Figure 2. Coronal sections and slices of the olfactory bulb of *Ambystoma mexicanum*. Columns left, central and right depict the Nissl-staining histological sections; the MRI images and the manual segmentation, respectively created from our template. (A) left and right single olfactory nerves; (B) the olfactory nerve (on), glomerular layer (g), and (C) mitral (m) and glomerular cell layers (gc).

cross contralaterally only after metamorphosis³⁴. The type of projections situated in the optic chiasm of neotenic and metamorphic axolotl is still unknown.

Mesencephalon. This section was subdivided into tectum, tegmentum and ventral hypothalamus. Since contrast was insufficient to differentiate between tectum and tegmentum, we manually segmented these structures using previously published drawings (Fig. 4C, Table 1). Optic tectum is the roof of the mesencephalon, and a big region in the salamander brain; it receives some nerves from the optic chiasm and processes visual signals in vertebrates³⁵. Tegmentum is located just ventrally from the optic tectum; from this region we were able to segment the interpeduncularis nucleus, which is known to integrate information for the limbic system³⁶. At the coronal level, the ventral hypothalamus appears as the lower area of the brain, physically separated from the optic tectum/tegmentum and surrounding the infundibulum (not segmented). However, the ventral hypothalamus becomes smaller in the left and right sides at posterior levels eventually disappearing, whereas the infundibulum increases in size. The third ventricle remains in the cerebral midline and the center of the optic tectum/tegmentum.

Rhombencephalon/pituitary. This is the most posterior area of the brain and contains regions such as the cerebellum and medulla oblongata. Cerebellum in amphibians is small in size with respect to other vertebrates³⁷,

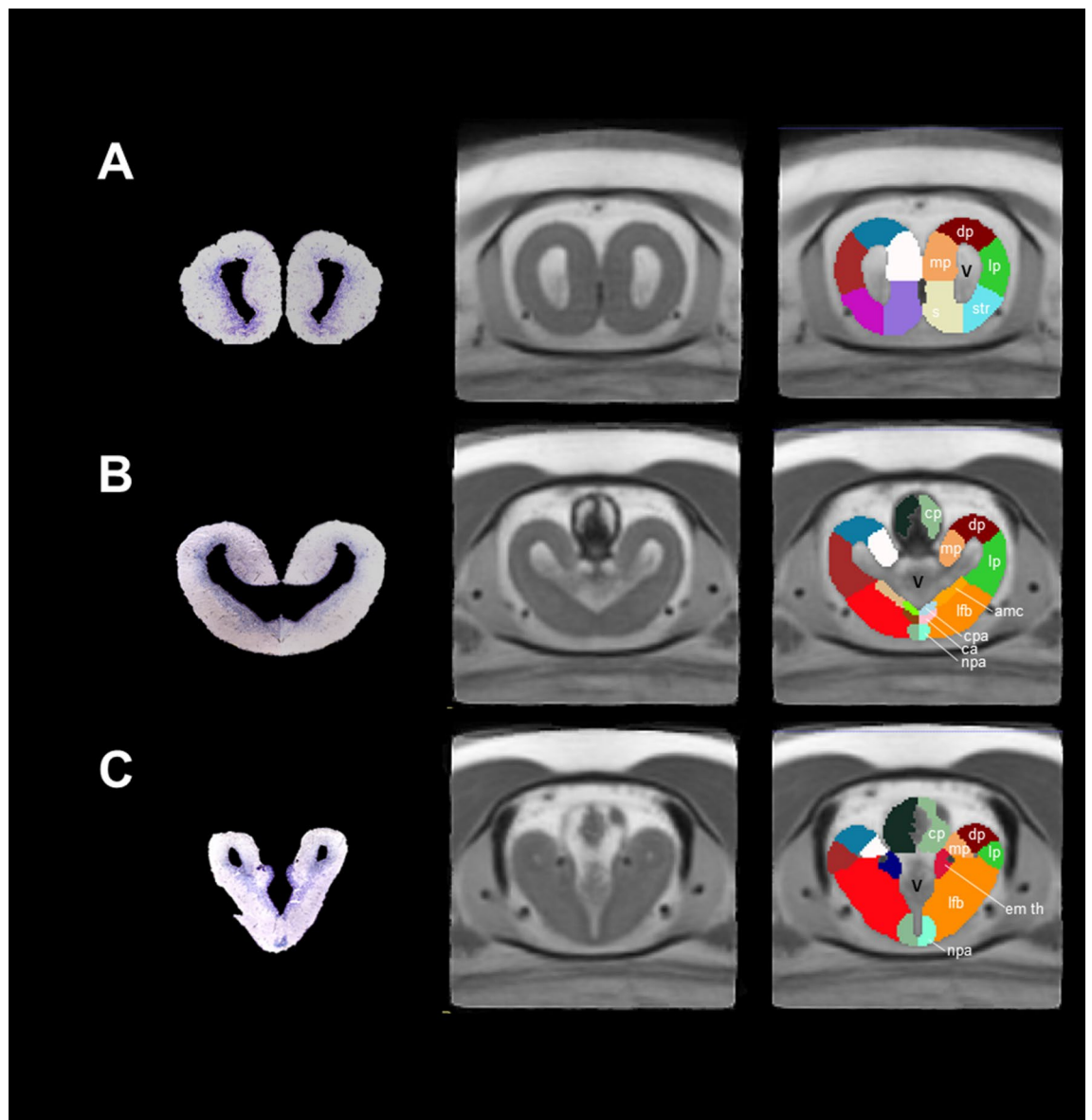


Figure 3. Coronal sections and slices of the telencephalon of *Ambystoma mexicanum*. Columns left, central and right depict the Nissl-staining histological sections; the MRI images and the manual segmentation, respectively created from our template. (A) dorsal (dp), lateral (lp) medial pallium (mp), striatum (str) and septum (s); (B) choroid plexus (cp), medial part of amygdala (amc), pallial (cpa) and anterior commissures (ca), and (C) thalamic eminence (em th) and anterior preoptic nuclei (npa). V ventricles.

a characteristic inversely correlated to the big genome of these species³⁸. As previously reported, we detected a small cerebellum in our MRI images (Fig. 5A). Medulla oblongata was identified as a single structure in the anterior rhombencephalon, but we were able to segment gray from white matter in the posterior rhombencephalon, according to differences in contrast in our MRI images and previous reports (Fig. 5B, Table 1). Moreover, we also recognized some cranial nerves such as nervous trigeminus (V), nervous lateralis anterior and nervus octavus (VIII) (Fig. 5B,C). Finally, we identified the pituitary gland, an endocrine organ which releases hormones in response to some peptides coming from hypothalamus^{39,40}. In our coronal sections, the pituitary gland appears at the lower part of the brain as the last visible signal of the ventral hypothalamus, increasing in size as it projects posteriorly to finally decrease and disappear (Fig. 5A).

Myelin rich regions in the axolotl CNS. Myelin is a characteristic of jawed vertebrate CNS^{41,42} which allows saltatory propagation of action potentials. Patterns of myelin rich regions are well-documented in mammals^{43–45} but in non-mammalian vertebrates, particularly in amphibians, the information is scarce. In an approach to identify myelin in the axolotl CNS, and due to its contribution to T2-weighted contrast in MRI, we performed specific myelin staining using the Black Gold II reagent in sagittal and coronal sections (Fig. 6A–D). Myelin-rich regions were evident in sagittal sections of the medulla oblongata, cerebellum, optic tectum and

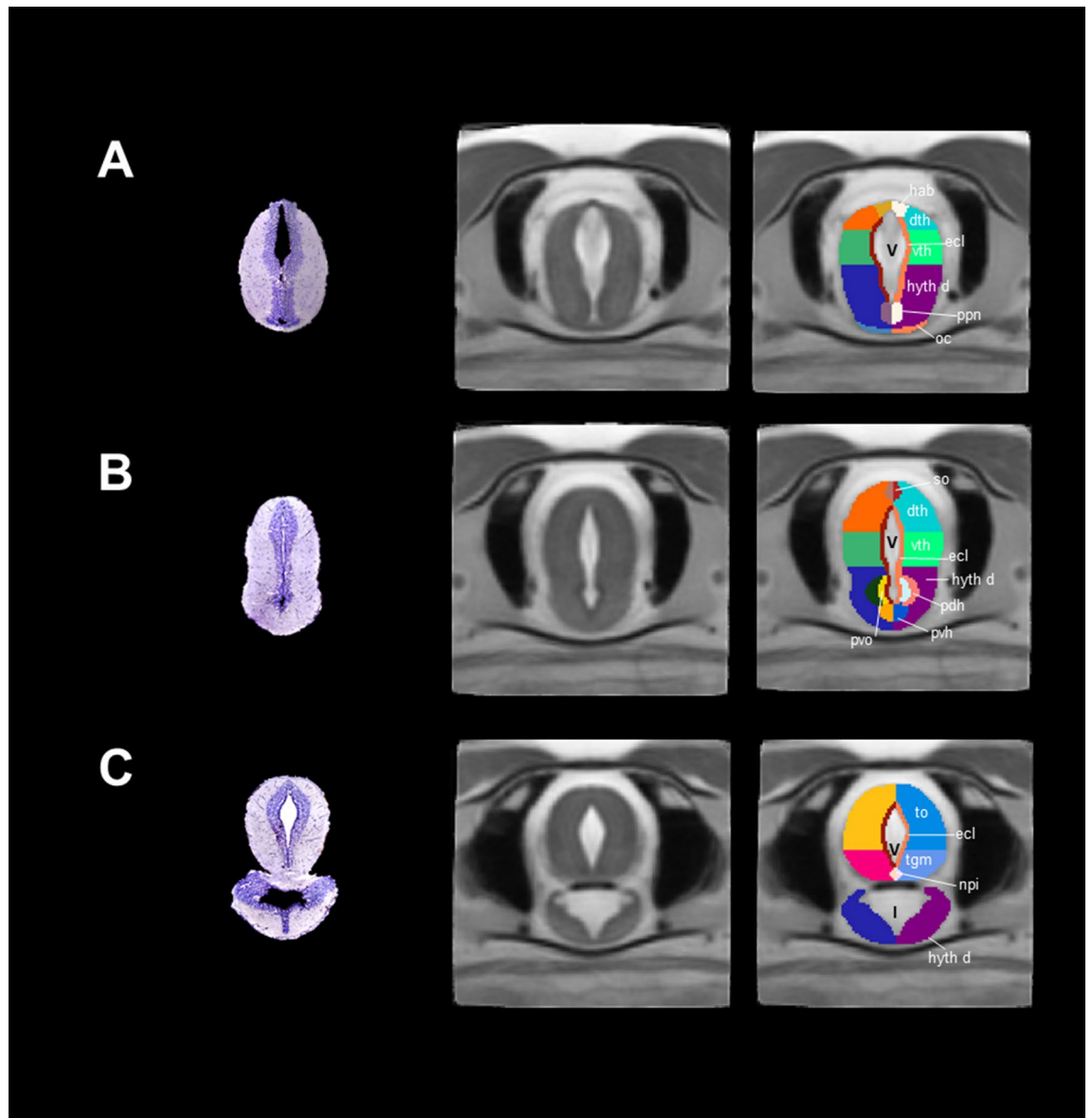


Figure 4. Coronal sections and slices of the diencephalon/mesencephalon of *Ambystoma mexicanum*. Columns left, central and right depict the Nissl-staining histological sections; the MRI images and the manual segmentation, respectively created from our template. (A) dorsal (dth) and ventral thalamus (vth), subcommissural organ (so), optic chiasm (oc), habenula (hab); (B) regions surrounding the floor of the third ventricle in the hypothalamus dorsalis (hyt d) such as the paraventricular organ (pvo), pars dorsalis (pdh) and pars ventralis hypothalami (pvh); (C) the mesencephalon, including the optic tectum (to), tegmentum (tgm) and interpeduncularis nucleus (npi). V ventricle, I infundibulum are indicated.

tegmentum (Fig. 6E–H); however, no myelin staining was observed in the anterior part of the brain, i.e., in the olfactory bulb and telencephalon (Fig. 6D). These results were confirmed using coronal sections, in which we are able to detect myelin in the lateral/medial forebrain bundle/amygdaloid complex (Fig. 7A), the ventral thalamus (Fig. 7B) and the optic tectum/tegmentum (Fig. 7C). Both, sagittal and coronal sections showed that medulla oblongata is a myelin rich region, particularly in the white matter, confirming the specificity of the myelin staining method (Fig. 7D). We were not able to detect myelin in the anterior part of the axolotl brain. This discrepancy could have different explanations. In the developing mammal, the myelination process starts in the spinal cord and gradually covers the posterior part of the CNS postnatally^{46,47}. It is possible that even if the juvenile stage of the axolotl brain is not fully myelinated, the adult brain could contain myelin in the anterior part of the brain. Another explanation could be that the axolotl lost the capacity to myelinate axons in the anterior part of the brain as result of neoteny and/or other unidentified physiological events. In this context, all amphibians go through dramatic transformations that occur in the transition from a pre- to a post metamorphic stage; however, axolotl can retain juvenile features throughout adulthood (neoteny/paedomorphism), resulting in adult (reproducing) individuals that maintain juvenile (larval) traits). Lastly, amphibian myelin composition might not be detected by Black Gold II. Even if this reagent is indeed myelin specific, amphibians have shown to present

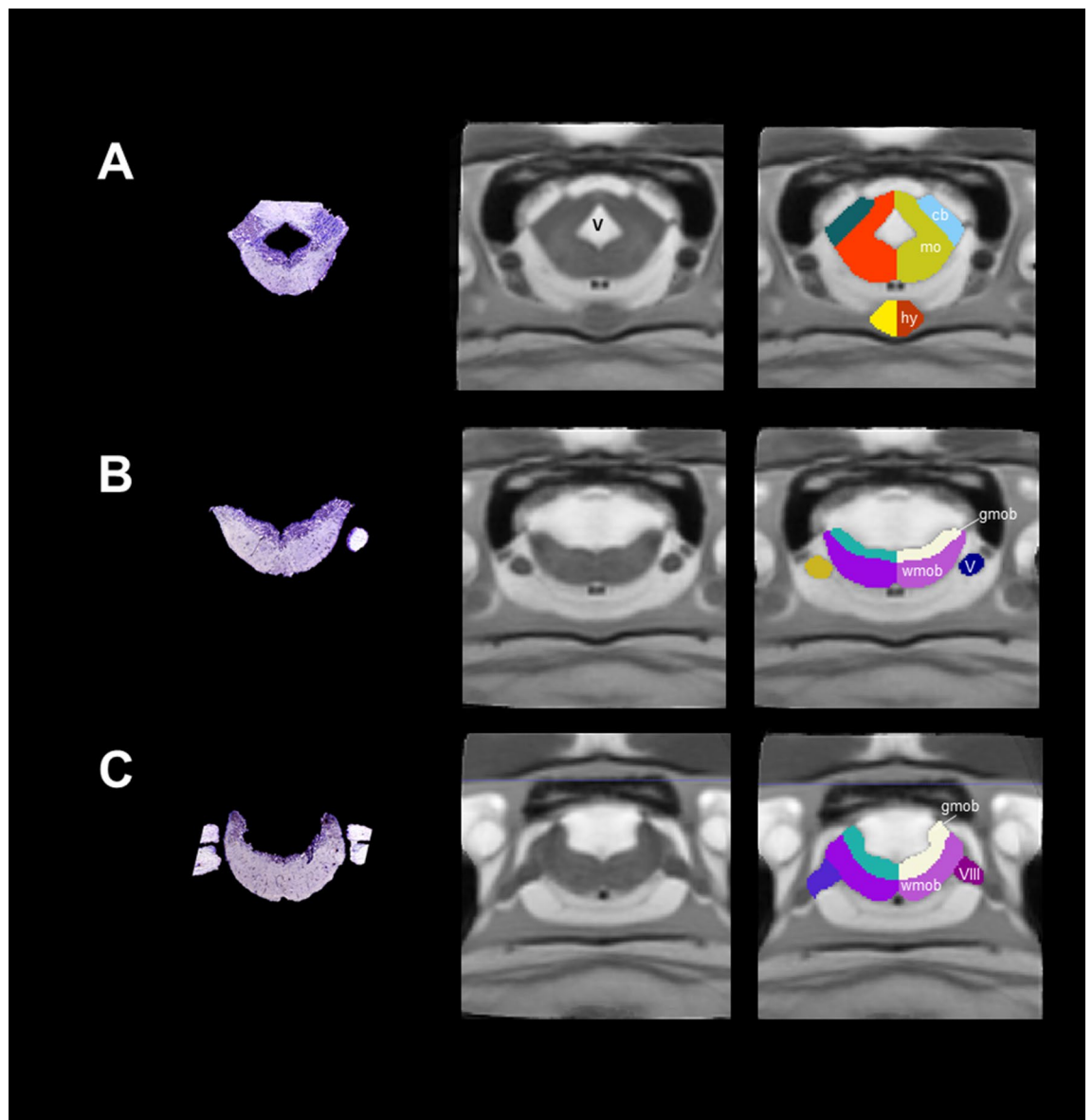


Figure 5. Coronal sections and slices of the medulla oblongata and pituitary gland of *Ambystoma mexicanum*. Columns left, central and right depict the Nissl-staining histological sections; the MRI images and the manual segmentation, respectively created from our template. (A) the rhombencephalon, where the cerebellum (cb), the medulla oblongata (mo) and the pituitary gland (hy) at the lower part of the brain are indicated; (B) white (wmob) and gray matter from medulla oblongata (gmob) and cranial nerves such as the nervous trigeminus (V), and (C) nervous lateralis anterior and nervus octavus (VIII).

different compositions of myelin in terms of lipid content^{48,49}. Therefore, it is plausible that axolotl could have a myelin that is not efficiently stained with Black Gold II in the anterior brain, at least at the stage of development that was analyzed in the present study. To confirm this last hypothesis, other stages of axolotl development and/or other methodologies to detect myelin could be tested.

Conclusions

The brain of vertebrates has been studied with different techniques, allowing researchers to visualize different aspects of its anatomy, according to the methodology employed. MRI of the axolotl brain allowed us to provide a 3D reconstruction of an amphibian brain and pituitary gland for the first time. In contrast with the results from histological sections, we were able to visualize native morphology of the brain structures and to transform this data in a 3D volume. Additionally, this is the first description of axolotl brain myelin distribution. Myelin rich regions were observed in the posterior, but not the anterior brain, a finding that deserves further attention. Overall, this work will provide a useful tool to explore new research avenues for the better understanding of this interesting endemic paedomorphic species, which is an important model in different research areas, including

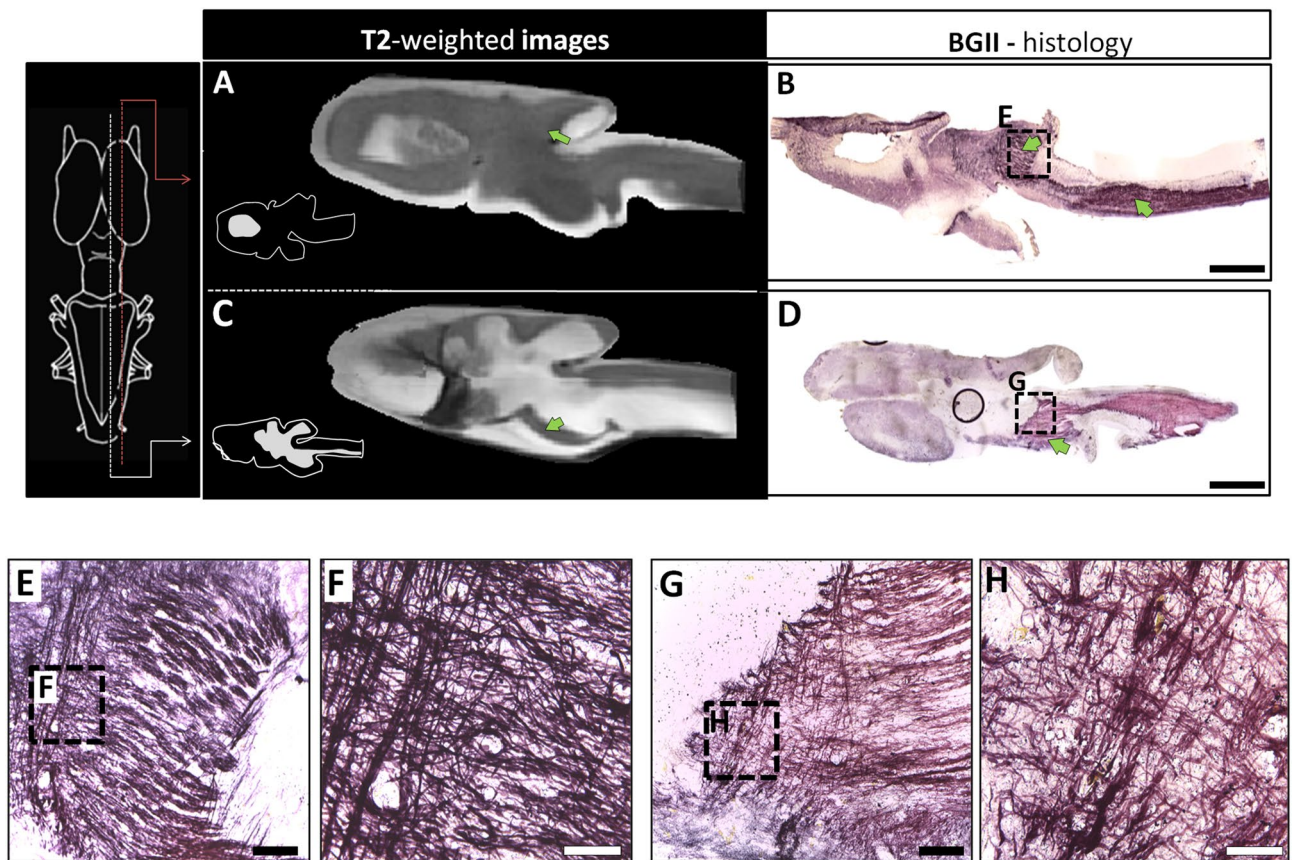


Figure 6. MRI and BGII techniques in the axolotl brain. (A, C) sagittal sections of in-vivo T2-weighted images and myelin staining with BGII; (B, D) the approximate myelin localization is indicated in the diagram on the left. Insets in (A) and (C) show diagrams of the corresponding sagittal plane. In the histological micrographs of BGII staining, (E) and (G) are amplifications of (B) and (D), while (F) and (H) are amplifications of (E) and (G), respectively. Bars in (B), (D) indicate 1 mm, in (E), (G) they indicate 100 μm , while in (F, H) they indicate 20 μm .

nervous tissue regeneration, and that is currently listed as critically endangered by the International Union for Conservation of Nature.

Materials and methods

Animals. Juvenile axolotls were kindly donated by Marco Terrones (Axolkali). All axolotls were maintained and handled in accordance with protocols approved by the Ethics for Research Committee of the Instituto de Neurobiología at the Universidad Nacional Autónoma de México (UNAM). The animal experiments were performed following the guidelines for use of live amphibians and reptiles in field and laboratory research of the American Society of Ichthyologists and Herpetologists. All the experiments complied with the ARRIVE guidelines.

Animals of around 3 months after hatching and weighing between 9 and 12 g were kept at our local housing for at least 20 days prior to imaging at 18 °C in 14/10 light/dark cycles. After habituation, animals were anesthetized by immersion with 0.4% tricain for 10–13 min.

MRI acquisition. MRI was performed on 20 animals at the National Laboratory for MRI, using a 7 T Bruker Biospec 70/16 scanner and a Helium-cooled two-channel rat-head coil (Bruker Cryoprobe). Once anesthetized, axolotls were placed in a plastic container and introduced in the scanner (Supplementary Fig. 2). A field map was first obtained and used for shimming of the main magnetic field. Next, images were acquired using a three-dimensionally encoded balanced steady-state gradient echo (True FISP) sequence with the following parameters: TR = 4.4 ms; TE = 2.2 ms; flip angle = 30°; NEX = 3; FOV = 20.48 × 15 × 10.24 mm³ and matrix = 256 × 188 × 128, yielding isometric voxel dimensions of 0.080 mm; scan time = 5 min 50 s. We also acquired diffusion-weighted images with a scan time of 11 min 44 s (not reported herein). Total scan time was 17 min 34 s.

MRI template construction. Individual image volumes were visually inspected for quality. Out of n = 20 images, n = 6 were rejected due to poor quality, with a final sample size of n = 14 for template construction. Images were converted from Bruker format to NIFTI using the software Bruker2nifti⁵⁰, and then from NIFTI to MINC using nii2mnc (<https://github.com/BIC-MNI/minc-toolkit-v2>). Several steps were followed to reach

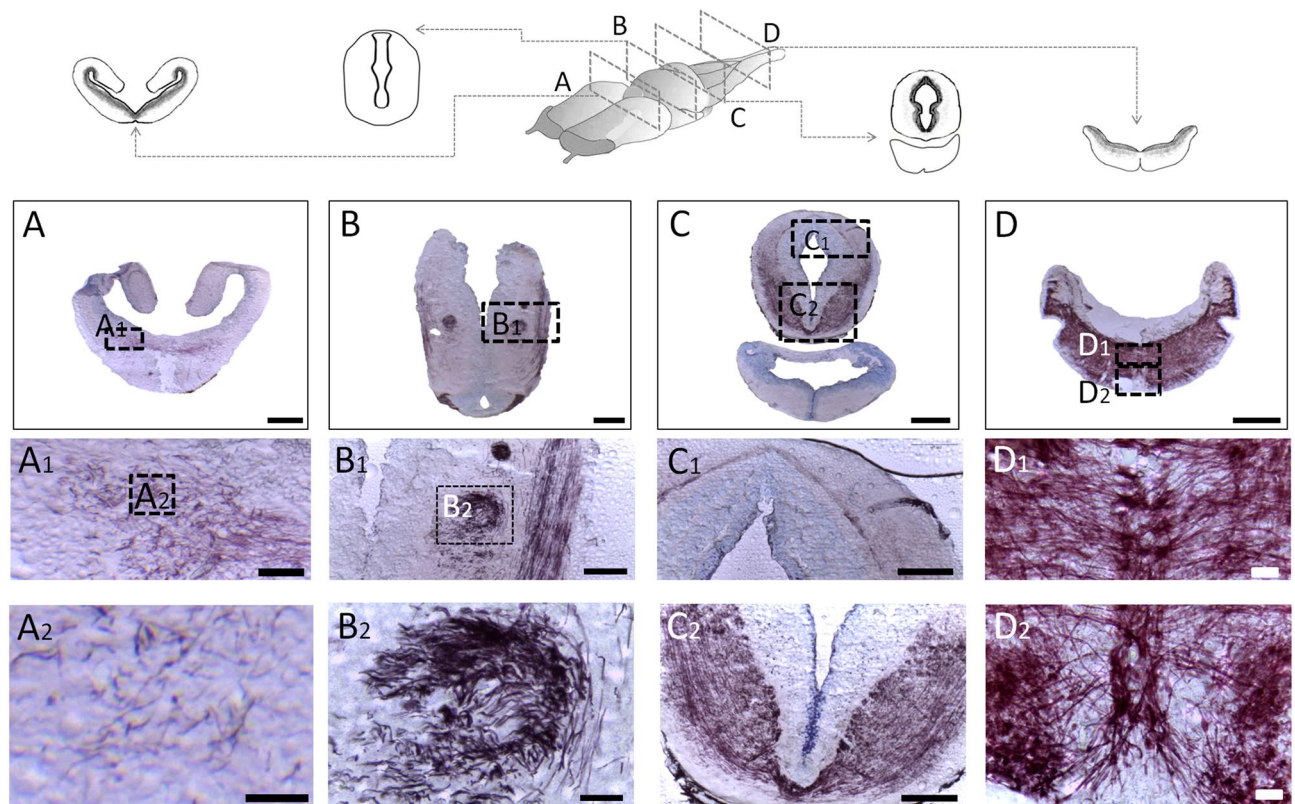


Figure 7. Myelination in the axolotl. Different coronal sections of the axolotl brain. (A) lateral/medial forebrain bundle/amygdaloid complex; (B) the dorsal thalamus; (C) the optic tectum/tegmentum, and (D) medulla oblongata. Below are amplifications for each section. Note the myelination gradient in the anteroposterior direction. The white matter of medulla oblongata is the structure with the greatest presence of myelin. The bars in the micrographs indicate 500 μm in (A–D), 100 μm in (A1, B1, C1, C2), and 20 μm in (A2, B2, D1, D2).

the final template construction. STEP1: each image was preprocessed using the following steps and commands; (1) cleaned header and center image to coordinate 0, 0, 0 (https://github.com/CoBrALab/minctoolkitextras/blob/master/clean_and_center_minc.pl); (2) reorientation to RAS: 90° rotation of the *y* axis using volrot; (3) *y* axis volume flip using volflip; and (4) N4 bias field correction using an Otsu mask⁵¹. STEP 2: we constructed a first template using the antsMultivariateTemplateConstruction2.sh script (<https://github.com/ANTsX/ANTs/blob/master/Scripts/antsMultivariateTemplateConstruction2.sh>)⁵². STEP 3: an initial brain mask was manually defined from the first template. STEP 4: fine tuning of the N4 correction and the first template; (1) inverse registration of the template brain mask to the native space for each subject; (2) reduce field of view to near brain (crop) using ExtractRegionFromImageByMask; (3) re-run the N4 bias field correction with the improved individual mask; (4) re-center the images; (5) rotation of the first template to a precise alignment with the axes. STEP 5: construction of the second template using the raw files and the first template as target. STEP 6: resampled second template from 0.08 × 0.08 × 0.08 mm to 0.06 × 0.06 × 0.06 mm. STEP 7: construction of the third template using the second template for warping. STEP 8: resampled final template from 0.06 × 0.06 × 0.06 mm to final resolution of 0.04 × 0.04 × 0.04 mm. STEP 9: construction of the final template using the third template for warping. The process is shown in Supplementary Fig. 3. Upsampling of the target templates was applied to increase model resolution⁵³.

MRI segmentation. Neuroanatomical segmentation was done manually drawing regions of interest (ROIs) using the ITK-SNAP (version 3.8.0)⁵⁴ on the final template (0.04 × 0.04 × 0.04 mm). We constructed two atlases: (1) 82-ROI atlas with sub-segmentation of pallium, telencephalon, tectum and rhombencephalon based on the available histological anatomic annotations and the nomenclature obtained from the different studies (Table 1), and (2) 64-ROI atlas without sub-segmentation of the pallium, telencephalon, tectum, and rhombencephalon (Supplementary Table 1). The ROIs were drawn over our final template while examining all three stereotaxic planes to reduce inconsistencies in delineation across slices. Labels were hierarchically constructed to simplify MRI analysis in higher resolutions. There are three levels that describe larger regions: (1) ROI; (2) embryological origin of the neural tube (olfactory bulb, telencephalon, diencephalon, mesencephalon, endocrine and rhombencephalon), and (3) hemispheres (right and left). Each ROI has a defined abbreviation. The atlas is openly available through Zenodo (<https://doi.org/10.5281/zenodo.4595016>).

Histological staining. For histological examination, brains were fixed in PFA (4%) and cryopreserved in sucrose (30%), then coronal or sagittal (40 μm) cryosections (one juvenile brain for every orientation) were cut

and mounted on electrocharged slides and stored at $-20\text{ }^{\circ}\text{C}$ until staining with the Black Gold II compound (EMD Millipore Corp., Billerica, MA, USA), using a modified protocol described by⁵⁵. Briefly, tissue sections were rehydrated in distilled water for about 2 min at RT. Then, the slides were incubated in 0.3% Black Gold II solution, dissolved in 0.9% saline vehicle (NaCl), and heated at $60\text{--}65\text{ }^{\circ}\text{C}$ for at least 40 min until the staining was complete. Next, the slides were rinsed for 2 min in Phosphate-Buffered Saline (PBS, RT), transferred to a 1% sodium thiosulfate solution for 3 min at $60\text{--}65\text{ }^{\circ}\text{C}$, and rinsed two or three times with distilled water. Sections stained with Black Gold II were counterstained with Nissl. Additional alternate slides were stained only with the Nissl protocol. For this, slides were transferred to a solution of 0.1–0.2% cresyl violet (blue; EMD Millipore Corp., Billerica, MA, USA) in 0.1% acetic acid for 5 min and then rinsed two times with distilled water. After, the tissue was dehydrated using sequential graduated alcohol solutions (50, 70 and 96%) and immersed in xylene for 1 min. The slides were then coverslipped with Entellan mounting medium.

Received: 10 December 2020; Accepted: 12 April 2021

Published online: 10 May 2021

References

- Voss, S. R. & Shaffer, H. B. Adaptive evolution via a major gene effect: Paedomorphosis in the Mexican axolotl. *Proc. Natl. Acad. Sci. USA* **94**, 14185–14189 (1997).
- Satoh, A., Mitogawa, K. & Makanae, A. Nerve roles in blastema induction and pattern formation in limb regeneration. *Int. J. Dev. Biol.* **62**, 605–612 (2018).
- Maden, M., Manwell, L. A. & Ormerod, B. K. Proliferation zones in the axolotl brain and regeneration of the telencephalon. *Neural Dev.* **8**, 1 (2013).
- Amamoto, R. *et al.* Adult axolotls can regenerate original neuronal diversity in response to brain injury. *Elife* **5**, e13998 (2016).
- Medina, L. & Abellán, A. Development and evolution of the pallium. *Semin. Cell Dev. Biol.* **20**, 698–711 (2009).
- Tazaki, A., Tanaka, E. M. & Fei, J.-F. Salamander spinal cord regeneration: The ultimate positive control in vertebrate spinal cord regeneration. *Dev. Biol.* **432**, 63–71 (2017).
- Lust, K. & Tanaka, E. M. A comparative perspective on brain regeneration in amphibians and teleost fish. *Dev. Neurobiol.* **79**, 424–436 (2019).
- Glasser, M. F. *et al.* The Human Connectome Project's neuroimaging approach. *Nat. Neurosci.* **19**, 1175–1187 (2016).
- Ma, Y. *et al.* A three-dimensional digital atlas database of the adult C57BL/6J mouse brain by magnetic resonance microscopy. *Neuroscience* **135**, 1203–1215 (2005).
- Valdés-Hernández, P. A. *et al.* An in vivo MRI template set for morphometry, tissue segmentation, and fMRI localization in rats. *Front. Neuroinform.* **5**, 26 (2011).
- Wisner, K., Odintsov, B., Brozoski, D. & Brozoski, T. J. Ratat1: A digital rat brain stereotaxic atlas derived from high-resolution MRI images scanned in three dimensions. *Front. Syst. Neurosci.* **10**, 64 (2016).
- Kovacević, N. *et al.* A three-dimensional MRI atlas of the mouse brain with estimates of the average and variability. *Cereb. Cortex* **15**, 639–645 (2005).
- Vellema, M., Verschuere, J., Van Meir, V. & Van der Linden, A. A customizable 3-dimensional digital atlas of the canary brain in multiple modalities. *Neuroimage* **57**, 352–361 (2011).
- Billings, B. K. *et al.* A three-dimensional digital atlas of the Nile crocodile (*Crocodylus niloticus*) forebrain. *Brain Struct. Funct.* **225**, 683–703 (2020).
- Hoops, D. *et al.* A 3D MRI-based atlas of a lizard brain. *J. Compar. Neurol.* **526**, 2511–2547 (2018).
- Ullmann, J. F. P., Cowin, G., Kurniawan, N. D. & Collin, S. P. A three-dimensional digital atlas of the zebrafish brain. *Neuroimage* **51**, 76–82 (2010).
- Simões, J. M., Teles, M. C., Oliveira, R. F., Van der Linden, A. & Verhoye, M. A three-dimensional stereotaxic MRI brain atlas of the cichlid fish *Oreochromis mossambicus*. *PLoS ONE* **7**, e44086 (2012).
- Herrick, C. J. *The Brain of the Tiger Salamander, Ambystoma tigrinum*. (University of Chicago Press, Chicago, 1948).
- Wang, H. H., Li, L. Y., Wang, L. W. & Liang, C. C. Morphological and histological studies on the telencephalon of the salamander *Onychodactylus fischeri*. *Neurosci. Bull.* **23**(3), 170–174 (2007).
- Mühlenbrock-Lenter, S., Roth, G. & Laberge, F. Evolution of the Pallium in Amphibians. In *Encyclopedia of Neuroscience* (eds Binder, M. D. *et al.*) (Springer, 2009).
- Clairambault, P. *et al.* Organization of the serotonergic system in the brain of two amphibian species, *Ambystoma mexicanum* (Urodela) and *Typhlonectes compressicauda* (Gymnophiona). *Anat. Embryol.* **190**, 87–99 (1994).
- Laberge, F., Mühlenbrock-Lenter, S., Grunwald, W. & Roth, G. Evolution of the Amygdala: New insights from studies in Amphibians. *Brain Behav. Evol.* **67**, 177–187 (2006).
- Krug, L., Wicht, H. & Northcutt, R. G. Afferent and efferent connections of the thalamic eminence in the axolotl *Ambystoma mexicanum*. *Neurosci. Lett.* **149**(2), 145–148 (1993).
- Beltramo, M. *et al.* Immunolocalization of aromatic L-amino acid decarboxylase, tyrosine hydroxylase, dopamine, and serotonin in the forebrain of *Ambystoma mexicanum*. *J. Comp. Neurol.* **391**(2), 227–247 (1998).
- Dicke, U., Wallstein, M. & Roth, G. 5-HT-like immunoreactivity in the brains of plethodontid and salamandrid salamanders (*Hydromantes italicus*, *Hydromantes genei*, *Plethodon jordani*, *Desmognathus ochrophaeus*, *Pleurodeles waltli*): An immunohistochemical and biocytin double-labelling study. *Cell Tissue Res.* **287**, 513–523 (1997).
- Bidaud, I. *et al.* Distribution of the mRNAs encoding the thyrotropin-releasing hormone (TRH) precursor and three TRH receptors in the brain and pituitary of *Xenopus laevis*: Effect of background color adaptation on TRH and TRH receptor gene expression. *J. Comp. Neurol.* **477**(1), 11–28. <https://doi.org/10.1002/cne.20235> (2004) (PMID: 15281077).
- Nagayama, S., Homma, R. & Imamura, F. Neuronal organization of olfactory bulb circuits. *Front. Neural Circ.* **8**, 98 (2014).
- Bill, B. R. & Korzh, V. Choroid plexus in developmental and evolutionary perspective. *Front. Neurosci.* **8**, 363 (2014).
- Freudenmacher, L., von Twickel, A. & Walkowiak, W. The habenula as an evolutionary conserved link between basal ganglia, limbic, and sensory systems—A phylogenetic comparison based on anuran amphibians. *J. Comp. Neurol.* **528**, 705–728 (2020).
- Meinl, A. The secretory ependymal cells of the subcommissural organ: Which role in hydrocephalus? *Int. J. Biochem. Cell Biol.* **39**, 463–468 (2007).
- Hodos, W. Evolution of the hypothalamus in anamniotes. In *Encyclopedia of Neuroscience* (eds Binder, M. D., Hirokawa, N. & Windhorst, U.) 1361–1363 (Springer-Verlag, Berlin, Heidelberg, 2008).
- Larsson, M. Binocular vision, the optic chiasm, and their associations with vertebrate motor behavior. *Front. Ecol. Evol.* **3**, 89 (2015).

33. Larsson, M. The optic chiasm: A turning point in the evolution of eye/hand coordination. *Front. Zool.* **10**, 41 (2013).
34. Jeffery, G. & Erskine, L. Variations in the architecture and development of the vertebrate optic chiasm. *Prog. Retin. Eye Res.* **24**, 721–753 (2005).
35. Ingle, D. J. Optic tectum. *Compar. Neurosci. Neurobiol.* https://doi.org/10.1007/978-1-4899-6776-3_40 (1988).
36. Morley, B. J. The interpeduncular nucleus. *Int. Rev. Neurobiol.* **28**, 157–182 (1986).
37. Butts, T., Modrell, M. S., Baker, C. V. H. & Wingate, R. J. T. The evolution of the vertebrate cerebellum: Absence of a proliferative external granule layer in a non-teleost ray-finned fish. *Evol. Dev.* **16**, 92–100 (2014).
38. Roth, G. & Walkowiak, W. The influence of genome and cell size on brain morphology in amphibians. *Cold Spring Harb. Perspect. Biol.* **7**, a019075 (2015).
39. Sower, S. A. Breaking dogma on the hypothalamic-pituitary anatomical relations in vertebrates. *Endocrinology* **156**, 3882–3884 (2015).
40. Lazcano, I. *et al.* Evolution of thyrotropin-releasing factor extracellular communication units. *General Compar. Endocrinol.* <https://doi.org/10.1016/j.ygcen.2020.113642> (2020).
41. Preston, M. A. & Macklin, W. B. Zebrafish as a model to investigate CNS myelination. *Glia* **63**, 177–193 (2015).
42. Czopka, T. Insights into mechanisms of central nervous system myelination using zebrafish. *Glia* **64**, 333–349 (2016).
43. Ibarrola, N. & Rodríguez-Peña, A. Hypothyroidism coordinately and transiently affects myelin protein gene expression in most rat brain regions during postnatal development. *Brain Res.* **752**, 285–293 (1997).
44. Barradas, P. C., Vieira, R. S. & De Freitas, M. S. Selective effect of hypothyroidism on expression of myelin markers during development. *J. Neurosci. Res.* **66**, 254–261 (2001).
45. Downes, N. & Mullins, P. The development of myelin in the brain of the juvenile rat. *Toxicol. Pathol.* **42**, 913–922 (2014).
46. Jacque, C. M., Collet, A., Raoul, M., Monge, M. & Gumpel, M. Functional maturation of the oligodendrocytes and myelin basic protein expression in the olfactory bulb of the mouse. *Dev. Brain Res.* **21**, 277–282 (1985).
47. Verity, A. N. & Campagnoni, A. T. Regional expression of myelin protein genes in the developing mouse brain: in situ hybridization studies. *J. Neurosci. Res.* **21**, 238–248 (1988).
48. Ki, P. F. & Kishimoto, Y. The lipid composition of urodele myelin which lacks hydroxycerebroside and hydroxysulfatide. *J. Neurochem.* **42**, 994–1000 (1984).
49. Ki, P. F., Kishimoto, Y., Stanley, E. F. & Griffin, J. W. Structure and function of urodele myelin lacking alpha-hydroxy fatty acid-containing galactosphingolipids: Slow nerve conduction and unusual myelin thickness. *Brain Res.* **345**, 19–24 (1985).
50. Ferraris, S. *et al.* Bruker2nifti: Magnetic resonance images converter from Bruker ParaVision to NIFTI format. *J. Open Source Softw.* **2**, 354 (2017).
51. Tustison, N. J. *et al.* N4ITK: Improved N3 bias correction. *IEEE Trans. Med. Imaging* **29**, 1310–1320 (2010).
52. Avants, B. B. *et al.* A reproducible evaluation of ANTs similarity metric performance in brain image registration. *Neuroimage* **54**, 2033–2044 (2011).
53. Janke, A. L. & Ullmann, J. F. P. Robust methods to create ex vivo minimum deformation atlases for brain mapping. *Methods* **73**, 18–26 (2015).
54. Yushkevich, P. A. *et al.* User-guided 3D active contour segmentation of anatomical structures: Significantly improved efficiency and reliability. *Neuroimage* **31**, 1116–1128 (2006).
55. Schmued, L. *et al.* Introducing Black-Gold II, a highly soluble gold phosphate complex with several unique advantages for the histochemical localization of myelin. *Brain Res.* **1229**, 210–217 (2008).

Acknowledgements

The authors would like to thank the technical assistance of M. C. Patricia Villalobos, Guadalupe Yasmín Hernández Linares, M.C. Leopoldo González Santos, Carlos S. Flores and Dr. Ericka A. de los Ríos. This work received support from Luis A. Aguilar (Laboratorio Nacional de Visualización Científica Avanzada), and the Laboratorio Nacional de Imagenología por Resonancia Magnética. We would also like to thank Gabriel A. Devenyi for his support. This work was supported by a Grant from PAPIIT IN204920.

Author contributions

I.L.: Conceptualization, methodology, investigation, writing—review and editing, formal analysis, resources, writing—original draft, writing—review and editing, visualization. A.C.M.: Methodology, investigation, writing—review and editing, visualization. L.C.: Conceptualization, writing—review and editing, supervision. J.J.O.R.: Methodology, investigation. E.A.G.V.: Conceptualization, methodology, software, formal analysis, resources, writing—original draft, writing—review and editing, visualization. A.O.: Conceptualization, project administration, supervision, funding acquisition, writing—original draft, writing—review and editing, visualization.

Competing interests

The authors declare no competing interests.

Additional information

Supplementary Information The online version contains supplementary material available at <https://doi.org/10.1038/s41598-021-89357-3>.

Correspondence and requests for materials should be addressed to I.L. or E.A.G.-V.

Reprints and permissions information is available at www.nature.com/reprints.

Publisher's note Springer Nature remains neutral with regard to jurisdictional claims in published maps and institutional affiliations.



Open Access This article is licensed under a Creative Commons Attribution 4.0 International License, which permits use, sharing, adaptation, distribution and reproduction in any medium or format, as long as you give appropriate credit to the original author(s) and the source, provide a link to the Creative Commons licence, and indicate if changes were made. The images or other third party material in this article are included in the article's Creative Commons licence, unless indicated otherwise in a credit line to the material. If material is not included in the article's Creative Commons licence and your intended use is not permitted by statutory regulation or exceeds the permitted use, you will need to obtain permission directly from the copyright holder. To view a copy of this licence, visit <http://creativecommons.org/licenses/by/4.0/>.

© The Author(s) 2021